

Research Article

Working Mechanism of Nonresonance Friction in Driving Linear Piezoelectric Motors with Rigid Shaking Beam

Xifu Chen ¹, Qian Lu,¹ Weiqing Huang,² and Yin Wang ³

¹Yancheng Institute of Technology, Yancheng 224051, China

²Guangzhou University, Guangzhou 510006, China

³Huaqiao University, Xiamen 361021, China

Correspondence should be addressed to Xifu Chen; chenxiforyou@163.com

Received 27 July 2018; Revised 6 October 2018; Accepted 22 October 2018; Published 28 November 2018

Academic Editor: Arkadiusz Zak

Copyright © 2018 Xifu Chen et al. This is an open access article distributed under the Creative Commons Attribution License, which permits unrestricted use, distribution, and reproduction in any medium, provided the original work is properly cited.

A kind of nonresonance shaking beam motors is proposed with the advantages of simple structure, easy processing, and low cost due to its wide application prospects in precision positioning technology and precision instruments. The normal vibration model between the stator and slider is divided into contact and noncontact types to investigate the nonresonance friction drive principle for this motor. The microscopic kinematics model for stator protruding section and the interface friction model for motor systems during both operating stages are established. Accordingly, the trajectory of the stator protruding section consists of two different elliptical motions, which differ from those of resonance-type motors. The output characteristic of the nonresonance shaking beam motor is proposed under steady working conditions with reference to the research method of standing-wave-type ultrasonic motors. Numerical analysis is used to simulate the normal vibration and mechanical output characteristics of the motor. Experimental and theoretical data fitting validates the numerical analysis results and allows the future optimization of nonresonance-type motors.

1. Introduction

Piezoelectric actuators are characterized by high efficiency, high positioning accuracy, fast response, and good stability [1–3]; these devices are effective precision actuation technologies for precision instruments [4, 5], guidance technology [6], biomedicine [7], and high-technology fields [8, 9]. Resonance-type linear piezoelectric motors include a type of linear motor based on “shaking beam” principle. This motor is composed of two piezoelectric vibrators with a phase difference of 90° to cause two-phase longitudinal vibration, the coupling effect of which produces an elliptical trajectory at the protruding section [10, 11]. This motor type can be developed with two Langevin-type transducers or a pair of piezoelectric ceramics and has simple structure, easy processing, and low cost. However, the resonance frequency consistency of the two vibrators strongly depends on structural design and machining accuracy due to the resonance working condition [12].

When the Langevin-type transducers are substituted with a pair of piezoelectric stacks and the small-stiffness horn is

changed into a rigid beam, a different linear piezoelectric motor can be obtained in nonresonance working condition [13]. Piezoelectric stacks have the characteristics of high precision and large deformation in nonresonance state; therefore, the motor can operate under nonresonance condition. The motor has the same simple structure and low demand on processing precision compared with “shaking beam” motors.

Similar to resonance motors, nonresonance linear piezoelectric motors produce elliptical motion at protruding section. The friction between stator and slider transfers the microvibration of the stator into the macroscopic linear motion of the slider. The frictional contact characteristics of nonresonance linear piezoelectric motors are similar to those of standing-wave-type motors. Thus, a small contact area and an intermittent contact interface could couple dynamic characteristics with shock, vibration, and friction [14]. The friction drive principle of resonance-type motors has been investigated based on the analysis of the vibration modes of stator [15, 16] and on the friction model of the contact interface [17, 18]. However, the elliptical trajectory of nonresonance-type motors is not completely the same as

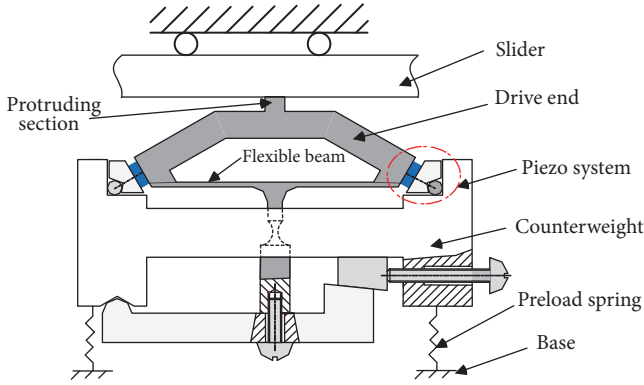


FIGURE 1: Schematic of the stator structure.

that of standing-wave-type motors, which is mainly determined by the distributed structural stiffness and excitation frequency [19]. The elliptical trajectory of nonresonance-type motors is significantly influenced by concentration structural stiffness and mass and nearly unrelated to the excitation frequency in the operating frequency range.

The friction between stator and slider exerts a pivotal effect on the motor mechanical performance. Accordingly, this study will focus on the characteristics of elliptical trajectories and the vibration characteristics of nonresonance-type motors and address the friction drive mechanism of this type of motors. With reference to the research method of the friction drive mechanism of standing wave motors, the longitudinal normal pressure and the tangential friction force on the interface between stator and slider will be obtained on the basis of the elliptical trajectory at the protruding section. The friction drive model of the motor can be produced for establishing the links between motor characteristics and structural and operation parameters. Thus, the research results can provide a theoretical model for nonresonance-type piezoelectric motors and predict the mechanical properties of this type of motors.

2. Motor Operating Mechanism

2.1. Formation of Elliptical Trajectory. The stator structure is shown in Figure 1, where the masses of drive end and counterweight are m_1 and m_2 , respectively; k_1 is the total stiffness of piezo system and flexible beam; and k_2 is the stiffness of preload spring.

Piezoelectric stacks can output large displacements in nonresonance state and sinusoidal displacements with the same frequency while excited by sinusoidal electric signals [20]. From the formation of elliptical trajectory under resonance condition, two piezoelectric stacks are excited by two sinusoidal voltages of phase difference $\pi/2$, as shown in Figure 2. Thus, two sinusoidal vibration displacements are obtained with quarter cycle phase difference. While the two displacements are simultaneously applied to a particular mechanism, the tangential displacement component (with a direction parallel to the slider movement) and the normal displacement component (with a direction perpendicular to

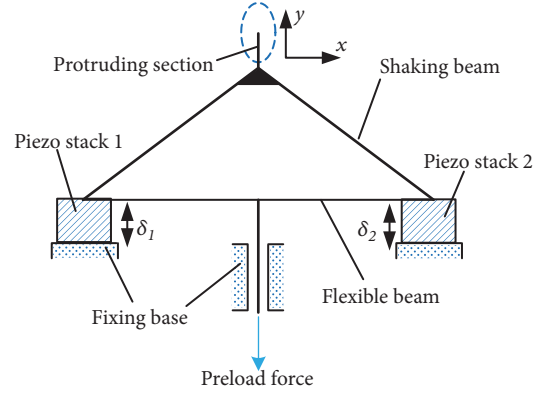


FIGURE 2: Structural model of drive foot.

the slider movement) are produced at the protruding section, which contribute to the elliptical trajectory of the protruding section in one excitation period.

In Figure 2, x direction represents the tangential direction, and y direction represents the normal direction. The output displacements of the two piezoelectric stacks are sinusoidal displacements in normal direction, called δ_1 and δ_2 , in two parallel y directions. We assume that $\delta_1 = A \sin \omega t$ and $\delta_2 = B \cos \omega t$, and the displacement parameter equations of the protruding section are

$$\begin{aligned} x &= \lambda (A \sin \omega t + B \cos \omega t) \\ y &= \lambda' (A \sin \omega t - B \cos \omega t) \end{aligned} \quad (1)$$

Thus, the elliptical trajectory is produced at the protruding section, as shown below:

$$\frac{x_0^2}{\lambda^2} + \frac{y_0^2}{\lambda'^2} = A^2 + B^2 \quad (2)$$

where λ is the tangential displacement scale factor and λ' is the normal displacement scale factor, both of which are constants associated with the geometric dimensions of drive foot.

As for nonresonance-type motors, the stator may be considered to consist of three parts, namely, drive foot, piezoelectric stacks, and the flexible structure that can be used for pretightening of piezoelectric stacks, and other mass parts (hereinafter referred to as ‘‘counterweight’’). Among the parts of stator, the piezoelectric stacks are mounted between the drive foot and the counterweight and pressed with preloads by the flexible structure. Given the micron-scale deformation of piezoelectric stacks and the flexible structure, they can be simplified as a linear spring with stiffness k_2 , as shown in Figure 4, which express the normal vibration model of the motor stator. In Figure 3, m_1 and m_2 are the masses of drive foot and counterweight, respectively; and $F_{1y}(t)$ and $F_{2y}(t)$ are the normal output force components of piezoelectric stacks.

In Figure 3, equivalent spring is the combination of the elastic structure and piezoelectric stacks, and its stiffness is expressed as k_1 with the link of $k_1 = k_T + k_S$, where k_T and k_S denote the stiffness of piezoelectric stacks and the

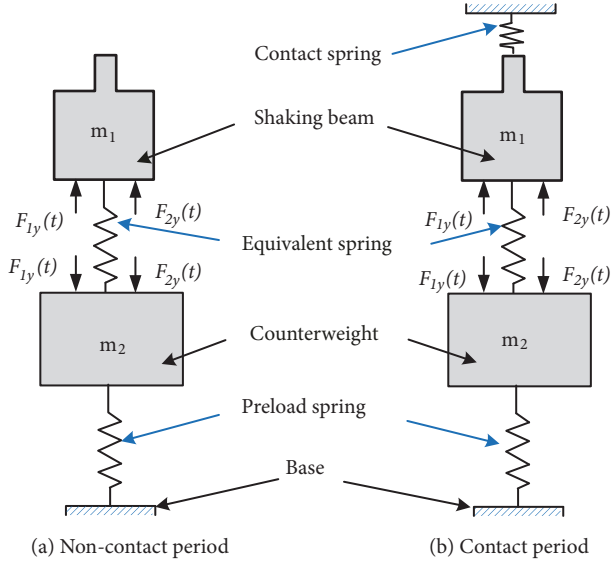


FIGURE 3: Normal vibration model of stator over the entire cycle.

elastic structure, respectively. The preload spring provides the prepressure between stator and slider, which is similar to ultrasonic motors, and its stiffness is represented by k_2 . In Figure 4(b), the contact deformation between stator and slider may be explained by the contact spring with the stiffness of k_3 . $k_3 = E_c A_c / h_c$, where E_c , A_c , and h_c denote the elastic modulus of friction plate bound on the stator, the contact area between stator and slider, and the thickness of the friction material, respectively [21]. From [20], the output force equation is as follows:

$$\begin{aligned} F_{1y}(t) &= \rho F_{max} \sin \omega t \\ F_{2y}(t) &= \rho' F_{max} \cos \omega t \end{aligned} \quad (3)$$

where F_{max} is the maximum output force of piezoelectric stacks; ω is the excitation frequency of piezoelectric stacks; and ρ and ρ' are the proportional coefficients and dependent on the structure size of the drive foot. The vibration differential equation of the stator during the noncontact stage is

$$\begin{aligned} \begin{pmatrix} m_1 & 0 \\ 0 & m_2 \end{pmatrix} \begin{pmatrix} \ddot{y}_1(t) \\ \ddot{y}_2(t) \end{pmatrix} + \begin{pmatrix} k_1 & -k_1 \\ -k_1 & k_1 + k_2 \end{pmatrix} \begin{pmatrix} y_1(t) \\ y_2(t) \end{pmatrix} \\ = \begin{pmatrix} F_{y1}(t) + F_{y2}(t) \\ -F_{y1}(t) - F_{y2}(t) \end{pmatrix} \end{aligned} \quad (4)$$

The amplitude of the protruding section is expressed as follows:

$$Y_n = \frac{F_{max}}{K_{en}} \quad (5)$$

where $K_{en} = ((k_1 - \omega^2 m_1)(k_2 - \omega^2 m_2) - \omega^2 m_1 k_1) / ((k_2 - \omega^2 m_2) / \sqrt{\rho^2 + \rho'^2})$.

The vibration differential equation of the stator during the contact stage is

$$\begin{aligned} \begin{pmatrix} m_1 & 0 \\ 0 & m_2 \end{pmatrix} \begin{pmatrix} \ddot{y}_1(t) \\ \ddot{y}_2(t) \end{pmatrix} + \begin{pmatrix} k_1 + k_3 & -k_1 \\ -k_1 & k_1 + k_2 \end{pmatrix} \begin{pmatrix} y_1(t) \\ y_2(t) \end{pmatrix} \\ = \begin{pmatrix} F_{y1}(t) + F_{y2}(t) \\ -F_{y1}(t) - F_{y2}(t) \end{pmatrix} \end{aligned} \quad (6)$$

The amplitude of the protruding section is as follows:

$$Y_C = \frac{F_{max}}{K_{ec}} \quad (7)$$

where $K_{ec} = ((k_1 + k_3 - \omega^2 m_1)(k_1 + k_2 - \omega^2 m_2) - k_1^2) / ((k_2 - \omega^2 m_2) / \sqrt{\rho^2 + \rho'^2})$.

2.2. Characteristics of Interfacial Force between Stator and Slider

2.2.1. Normal Contact Force. From the motor cycle, the normal contact force between stator and slider is periodically intermittent, similar to the elliptical trajectory of the resonance motor. When the motor is steadily running, the normal contact force exists during a certain period of time in a cycle, and thus the stator does work on the slider. However, the stator does not work on the slider, while the normal contact force is zero during another period of time in a cycle. The normal contact force between stator and slider depends on the normal displacement component of the protruding section. The noncontact angle θ_n is defined as $\theta_n = \theta_b - \theta_a$, as shown in Figure 4.

In Figure 4, the initial elastic deformation δ_0 between stator and slider caused by the deformation of preload spring is assumed; the displacement trajectory equation of the protruding section can be obtained by referring to the elliptical trajectory equation of the resonance-type motors [17].

$$\begin{aligned} x(t) &= -X_n \cos \omega t \\ y(t) &= Y_n \sin \omega t \end{aligned} \quad (8) \quad (y_T < \delta_0)$$

$$\begin{aligned} x(t) &= -X_c \cos \omega t \\ y(t) &= Y_c \sin \omega t \end{aligned} \quad (9) \quad (y_T \geq \delta_0)$$

Thus, the normal contact force between stator and slider can be expressed as

$$F_c = \begin{cases} 0, & (y(t) < \delta_0) \\ k_3 (y(t) - \delta_0), & (y(t) \geq \delta_0) \end{cases} \quad (10)$$

From Figure 5,

$$\delta_0 = -Y_c \cos \left(\frac{\theta_n}{2} \right) \quad (11)$$

Equation (11) is substituted into (10) in combination with Figure 5. Equation (10) can then be rewritten as formula (15).

When the motor works under steady state, the normal equilibrium position of the protruding section remains nearly unchanged. The normal contact force between stator and slider is $F_{c0} = k_c Y_c \cos(\theta_n/2)$. In one working cycle, the protruding section reciprocates near the equilibrium position in a way starting from the equilibrium position and returning to the equilibrium position. During the entire process, the total momentum of motor stator in the normal direction is a constant, and the external forces for the stator system include F_{c0} and F_0 . When the motor is stable, according to the principle of momentum conservation, the momentum generated by the contact force is equal to that generated by the preload in an entire cycle.

Therefore,

$$\int_t^{t+T} F_{c0} dt = F_0 \cdot T \quad (12)$$

$$F_c = \begin{cases} 0, & \frac{(3\pi - \theta_n)}{2} < \omega t < \frac{(3\pi + \theta_n)}{2} \\ k_c Y_c \left(\sin \omega t + \cos \left(\frac{\theta_n}{2} \right) \right), & 0 < \omega t < \frac{(3\pi - \theta_n)}{2}, \frac{(3\pi + \theta_n)}{2} < \omega t < 2\pi \end{cases} \quad (15)$$

2.2.2. Contact Interface Friction between Stator and Slider.

The relative motion between stator and slider is low-speed motion ($\mu\text{m/s}$ to mm/s); hence, the motor tribological behavior is a combination of slip motion and adhesion state according to tribological theory. Therefore, Coulomb friction model, with relatively simple parameters, is adopted in this situation and is shown in Figure 5, where F_s is the static friction, F_d is the dynamic friction, and F_v is the viscous friction.

On the basis of Coulomb friction model, the friction F_v can be expressed as follows:

$$F_v \approx \begin{cases} \varepsilon_c (\dot{x}_t - v_{pt}) + F_d, & \dot{x}_t - v_{pt} > 0 \\ F_e + m_e \ddot{x}_t, & \dot{x}_t - v_{pt} \equiv 0 \\ \varepsilon_c (\dot{x}_t - v_{pt}) - F_d, & \dot{x}_t - v_{pt} < 0 \end{cases} \quad (16)$$

In (16), $F_d = \mu_d F_c$, where μ_d is the dynamic friction coefficient of the friction pair between stator and slider, F_e is the external force that acts on the slider (excluding the inner frictional force of slider), and v_{pt} is the instantaneous velocity of slider. ε_c represents the viscous friction coefficient, and the oblique line in Figure 6 reflects the change in viscous frictional force F_v with relative velocity.

As for the motor system, the friction force F_v does a positive work and promotes the slider movement when $\dot{x}_t > v_{pt}$; however, it does a negative work and prevents the mover movement. When $\dot{x}_t = v_{pt}$, the contact interface is fully bonded, and no relative motion occurs between stator

Substituting (15) into (12), we can obtain

$$F_0 = k_c Y_c \left(1 - \frac{\theta_n}{2\pi} \right) \cos \frac{\theta_n}{2} \quad (13)$$

We assume that $\theta_c = 2\pi - \theta_n$, where θ_c corresponds to the contact angle of nonresonance-type motors, and (13) can be written as

$$F_0 = -k_c Y_c \frac{\theta_c}{2\pi} \cos \frac{\theta_c}{2} \quad (14)$$

From (14), $F_0 \leq 0$ when $0 < \theta_c \leq \pi$. Initial prepressure always exists between stator and slider, that is, $F_0 > 0$; therefore, $\pi < \theta_c \leq 2\pi$. The contact angle and preload increase under the same operating condition.

When the preload is zero, theoretically, the contact angle equals π . In practice, if no prepressure exists between stator and slider, the contact condition and the motor operation will be unstable due to such factors as the geometric tolerances of friction plate and the surface roughness of contact interface. When $F_c \geq k_c Y_c$, $\theta_c = 2\pi$, which means the constant contact between stator and slider during the entire working cycle.

and slider. Therefore, the magnitude and direction of the frictional force are cyclically changed during the operating process of motors.

2.3. Motor Output Characteristics in Steady State. Similar to the interfacial force characteristics of motor, the speed of the protruding section of stator is periodically changed during the steady working process. Therefore, the speed and acceleration of the mover are also changed periodically. In this way, the slider velocity is not constant in the entire cycle. However, the slider will reach a certain equilibrium velocity, called v_m , during the stable operation process due to the high-frequency coupling effect of the contact interface between stator and slider. Thus, the tangential vibration velocity of the protruding section at some moment is equal to the equilibrium velocity of slider; that is, some points, called equilibrium velocity points, exist in the contact domain, on which the velocity is equal to v_m . Figure 6 shows the influence of the speed of the protruding section on the work of stator, in which points P and P' are both equilibrium velocity points.

From Figure 6, we can obtain

$$\begin{aligned} \theta_p &= \arcsin \left(\frac{v_m}{\omega X_c} \right) \\ \theta_{p'} &= \pi - \arcsin \left(\frac{v_m}{\omega X_c} \right) \end{aligned} \quad (17)$$

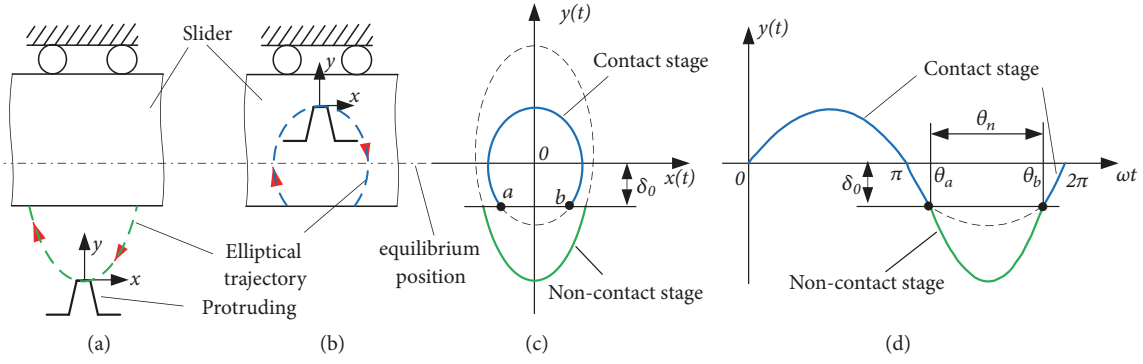


FIGURE 4: Motor contact model.

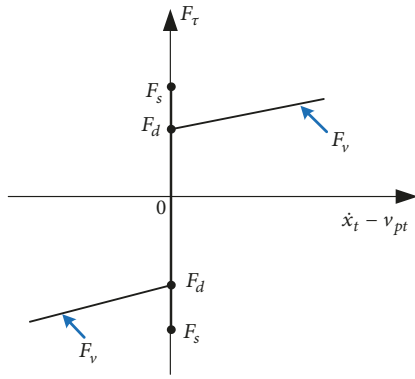


FIGURE 5: Coulomb friction model.

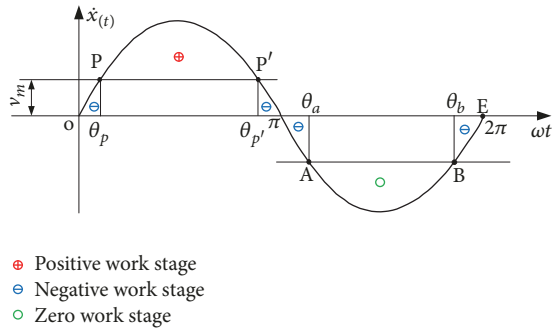


FIGURE 6: Relationship between the tangential vibration speed of the protruding section and the work of stator.

In the contact domain $[\theta_p, \theta_{p'}]$, the tangential speed of the protruding section is larger than v_m ; thus, the frictional force does a positive work. The stator drive end velocity is smaller than v_m in the contact domains $[\theta_c, \theta_p]$, $[\theta_{p'}, \theta_a]$, and $[\theta_b, \theta_c]$; therefore, the frictional force does a negative work. In the noncontact domain $[\theta_a, \theta_b]$, the stator does not work.

The energy loss caused by rail friction is disregarded, and the interfacial frictional force between stator and slider and the external load are taken as the external force. According to the work–energy theorem for systems, the increment of the system mechanical energy is equal to the total work by the

external force. The mechanical energy of the motor system does not change in a stable working cycle, and it can be obtained as (18).

$$\int_t^{t+T} (F_\tau - F_e) v_m dt = 0 \quad (18)$$

Accordingly,

$$F_e = \frac{1}{T} \int_t^{t+T} F_\tau dt \quad (19)$$

When $\pi < \theta_c < 2\pi$, given the equilibrium velocity is in the contact domain, we can have the following equations:

$$\begin{aligned} \theta_p &= \arcsin\left(\frac{v_m}{\omega x_Q}\right) > \theta_a; \\ 0 < \theta_c < 2 \arccos\left(\frac{v_m}{\omega x_Q}\right). \end{aligned} \quad (20)$$

The motor output force can be written as

$$\begin{aligned} F_e &= \frac{1}{2\pi} \int_{\theta_a}^{\theta_b} F_\tau d\omega t = \frac{1}{2\pi} \left(\int_0^{\theta_p} F_\tau d\omega t + \int_{\theta_p}^{\theta_{p'}} F_\tau d\omega t \right. \\ &+ \int_{\theta_{p'}}^{\theta_a} F_\tau d\omega t + \int_{\theta_b}^{2\pi} F_\tau d\omega t \left. \right) = \frac{1}{2\pi} \left(\int_{\theta_p}^{\theta_{p'}} F_\tau d\omega t \right. \\ &+ 2 \int_{\theta_{p'}}^{\theta_a} F_\tau d\omega t \left. \right) \quad (21) \end{aligned}$$

Substituting (16) and (17) into (21) yields

$$\begin{aligned} F_e &= \frac{1}{\pi} \left(\varepsilon_c \omega x_c - \Re \sin \frac{\theta_c}{2} \right) + \frac{2}{\pi \omega x_c} \Re \sqrt{\omega^2 x_c^2 - v_m^2} \\ &- \Re \cos \frac{\theta_c}{2} - \frac{\theta_c}{2\pi} \left(\varepsilon_c v_m - \Re \cos \frac{\theta_c}{2} \right) \\ &+ \frac{2}{\pi} \Re \cos \frac{\theta_c}{2} \arcsin \frac{v_m}{\omega x_c} \quad (22) \end{aligned}$$

where $\Re = \mu k_c y_c$.

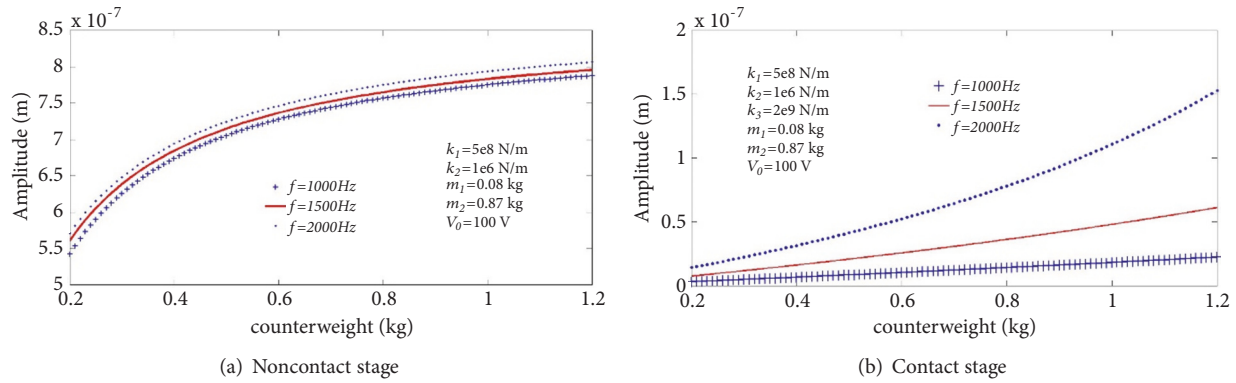


FIGURE 7: Relationship between normal amplitude and counterweight.

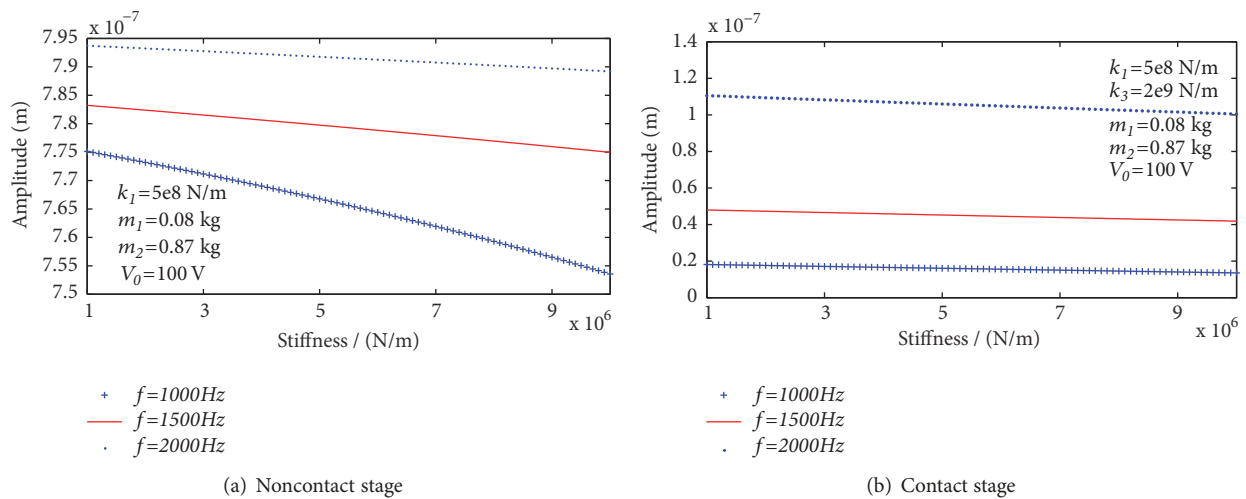


FIGURE 8: Relationship between normal amplitude and preload stiffness.

3. Simulation of Motor Performance

3.1. Simulation of Motor Vibration Characteristics. The main parameters of the stator vibration model are determined according to the structural parameters of the motor prototype. The piezoelectric stacks we use are PL055.30 type piezoelectric ceramics produced by PI company. The dimension of stack actuator is $5\text{mm} \times 5\text{mm} \times 2\text{mm}$. According to the technical data of PI company, when the amplitude of exciting voltage is 100V , it can elongate $2.2\ \mu\text{m}$.

Figures 7(a) and 7(b) illustrate the influence of counterweight on the stator vibration characteristics in noncontact and contact stages, respectively. In the two figures, the normal amplitude of the protruding section increases as the counterweight increases. When the counterweight ranges from 0.2 kg to 0.8 kg , it exerts minimal effects on the amplitude in both stages. However, the normal magnitudes are similar to one another under different excitation frequencies in the noncontact stage but are different in the contact stage.

As shown in Figures 8(a) and 8(b), the effects of preload spring stiffness on the normal amplitude of the protruding section are investigated for the motor system in the noncontact and contact stages, respectively. The normal amplitude is

nearly constant in the noncontact and contact stages under a certain excitation frequency. Particularly, the amplitude varies from $0.75\ \mu\text{m}$ to $0.79\ \mu\text{m}$ with excitation frequencies of $1, 1.5,$ and 2 kHz when the counterweight changes from 0.2 kg to 1.2 kg .

The simulation results imply that the counterweight has a significant influence on the normal vibration characteristics of the motor system, whereas the stiffness of the preload spring exerts a minimal effect. From the simulation for contact and noncontact stages, the counterweight ranges from 0.7 kg to 1 kg . However, the amplitude of the resonance motor depends mainly on the excitation voltage, the excitation frequency, and the vibration mode of motor stator. Therefore, the mass of counterweight has little effect on the amplitude of a resonant motor.

A small stiffness value of approximately $2 \times 10^6\text{ N/m}$ is selected considering the regulation effect of the preload spring on the contact state between stator and the mover. Contact stiffness has a great influence on motor performance and the longitudinal amplitude characteristics of protruding section. Ceramic friction materials are necessary to use to produce a large contact stiffness considering the large contact stiffness can improve the output force of the motor.

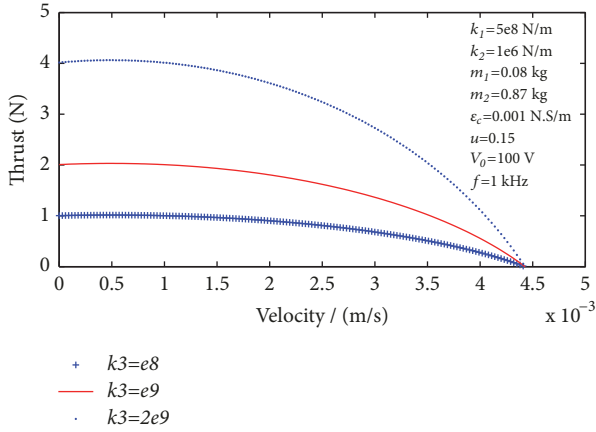


FIGURE 9: Effect of the contact stiffness of motor.

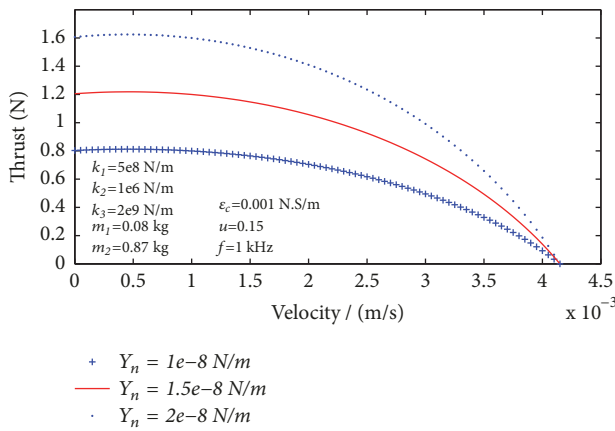


FIGURE 10: Effect of the normal amplitude of motor.

3.2. *Simulation of Motor Characteristics in Steady State.* Figure 9 illustrates the effect of contact stiffness on motor characteristics in steady state. Three types of contact stiffness represent three different hardness friction materials, namely, ceramic, 45 steel, and epoxy friction material, with the corresponding contact stiffness of 2×10^9 , 10^9 , and 5×10^8 N/m, respectively. The maximum output force increases with the increase in contact stiffness. When utilizing the friction material with large stiffness, the maximum output force of the motor can be more than 4 N. However, if the friction material with small stiffness is employed, the maximum motor thrust is only approximately 1 N.

Figure 10 shows the effect of normal amplitude on the motor characteristics in steady state. When exciting piezoelectric stacks with different voltages of 50, 75, and 100 V and with an excitation frequency of 1 kHz, the corresponding normal amplitudes are approximately 10, 15, and 20 nm, respectively, during the contact stage. The maximum output force increases when the normal amplitude is large, and the large normal amplitude results in hard mechanical properties for motor.

From Figures 9 and 10, the motor maximum velocity is more than 4 mm/s with zero load, and the maximum motor thrust can be up to 4 N when the motor velocity is zero.

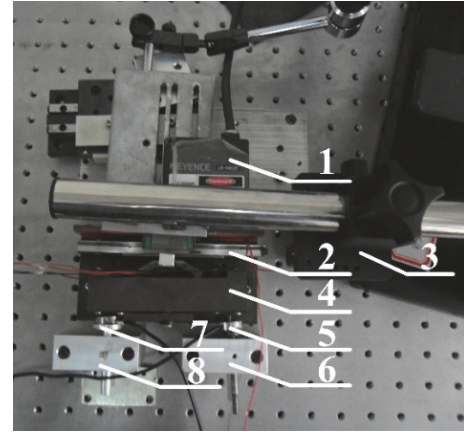


FIGURE 11: Microscopic displacement test system.

4. Experiment

4.1. *Prototype Structure and Experimental Test System.* Figure 11 shows the microscopic displacement test system for the normal amplitude of protruding section and the motion of slider. The normal and tangential displacement sensors are the LK-H020 laser displacement sensor from KEYENCE Company with an accuracy of 10 nm. The pressure sensor is an LC1015-type pressure sensor with an accuracy of 0.2 N.

There are 1 normal displacement sensor, 2 sliders, 3 tangential displacement sensors, 4 stators, 5 right pressure sensors, 6 right fixed blocks, 7 left pressure sensors, and 8 left fixed blocks.

4.2. *Motor Stator Amplitude Experiments.* As shown in Figure 12, a laser displacement sensor controller is employed to realize data transmission and test mode control between laser heads and host computer for measuring the normal amplitude of protruding section and the microscopic motion characteristic of slider. Laser displacement sensors have a sampling frequency of 50 kHz; therefore, a large amount of data may be obtained and transmitted to the host computer. In this way, we can import these data into the numerical analysis software for data processing, which makes the normal vibration displacement curve available.

The vibration displacement at the protruding section under different excitation conditions is tested on the basis of the above principle. The normal vibration displacement curves are tested under an excitation signal of 70 V and 600 Hz and an excitation signal of 90 V and 1400 Hz, respectively, as shown in Figures 13(a) and 13(b), respectively. The detailed measurement methods are indicated in another reference document [13].

The two figures depict that the normal vibration displacement curve of the protruding section is also approximately sinusoidal, and the vibration displacement period coincides with the period of the excitation voltage. However, the random vibration from the external environment exerts a great influence on individual experimental points because the laser displacement sensor is highly sensitive to the external environment, which reduces the fitting accuracy. Therefore,

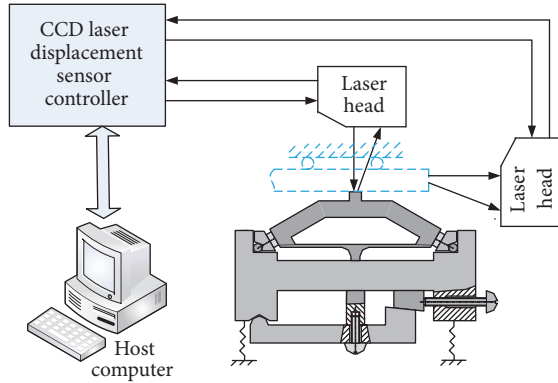


FIGURE 12: Microscopic displacement test principle.

the displacement tests should be carried out on the vibration isolation platform. Thus, the external environment has little effect on the measured experimental data and then vibration displacement curves with minimal noise could be obtained.

The amplitude–frequency curves can be obtained according to the normal vibration displacement curves at different exciting frequencies, as shown in Figure 14.

Figure 14 illustrates the comparison characteristics between the simulation curves and experimental data of the normal amplitude–frequency response under excitation voltages of 70 and 90 V. With the same excitation voltage, the amplitude increases with the increase in frequency in the frequency range from 1 kHz to 2 kHz. The error of the normal amplitude is small (approximately 1% to 3%), which is beneficial to realizing motor stability in the wide-frequency domain. The experimental amplitude curve is slightly larger than the simulation value. The main reason lies in that external environmental interference causes the numerical range expansion of the measurement data, which leads to a slight increase in amplitude value during the fitting process.

4.3. Experiments on Motor Mechanical Characteristics. The first two resonance frequencies of the motor are 230 Hz and 3.17 kHz, respectively. Theoretically, the motor operates between the first-order mode and the second-order mode. Experiment results show that the motor runs in the frequency range between 500 Hz and 2.2 kHz. When the frequency is higher than 2.2 kHz, the current of the power amplifier drops sharply, and the piezoelectric stack cannot work properly.

The motor mechanical properties can be specified as the thrust and velocity of the motor. The velocity can be obtained from the displacement curve of slider, which is produced in a similar way of normal vibration displacement curves with the laser displacement sensor system. The output force experiment of motor is performed with the traditional hanging weight method.

Figure 15 shows that when the prepressures are 10 and 16 N, the displacement curve of the slider presents perfect straight lines, which indicates that the motor is running stably. However, when the prepressure is 3 N, the displacement curve of the motor shows an irregular curve along a similarly linearity line, which indicates that the motor is running in an

unsteady station. Practically, the main reason lies in the shape error and surface roughness of the interface between stator and slider, which leads to a poor contact condition between stator and slider when the prepressure is significantly small. Consequently, the output speed of the motor is available by calculating the average velocity of the slider from the displacement curves.

The mechanical characteristics of the motor are experimented and simulated when the excitation voltage is 100 V and the excitation frequency is 1.5 kHz. With precision hard ceramic as the frictional material of the slider, the contact stiffness is 2×10^9 N/m. The viscous friction coefficient was tested and its value varies from 0.0005 N.s/m to 0.005 N.s/m. Since the velocity of the motor is very low, when ε_c is in the range of 0.0005 N.s/m to 0.005 N.s/m, the viscous friction coefficient has little effect on the mechanical characteristics of the motor. Therefore, the value of ε_c is taken as 0.001 N.s/m. Figure 16 shows the simulation curve and experimental data of the motor mechanical characteristics with prepressures of 10 and 16 N. The simulation and experimental results show that the motor has a hard mechanical property when the prepressure is 16 N with the maximum output force of approximately 4.5 N, which is approximately 1.5 times of that when the prepressure is 10 N. The motor no-load velocity is approximately 2.5 mm/s, whether the prepressure is 10 N or 16 N.

Small errors are determined between the theoretical and experimental results. The maximum speed and thrust from the experiment are smaller than those from the theoretical simulation results. This difference is due to the inner friction that exists in the slider system and the assembly error of the stator, which will reduce the motor performance. However, the simulation curves reflect the trends of motor performance generally and can provide performance prediction and optimization method for the structure design.

According to the normal contact model of stator and mover, the contact angle will be up to 2π when the prepressure increases to a certain critical value, which is approximately 20 N for the prototype. The slide velocity will be reduced rapidly, and the slider makes the reciprocating motion with the prepressure of above 25 N. When the prepressure is between 5 and 16 N, the optimal performance of the motor can be obtained with the maximum velocity of 5 mm/s and the maximum thrust of 4.2 N. However, when the prepressure is less than 3 N, the motor operates in unstable state due to the existence of assembly error and geometric tolerances, which cause different contact conditions between stator and slider at different contact positions.

5. Conclusion

A nonresonance “shaking beam”-type linear piezoelectric motor is proposed, and the motion characteristics of the motor stator are studied. Unlike a resonance-type motor, the trajectory of stator protruding section consists of two different elliptical arcs, which are the trajectories in contact and noncontact stages.

A normal vibration model between stator and slider is established for contact and noncontact stages. The numerical analysis method is used to simulate the normal vibration

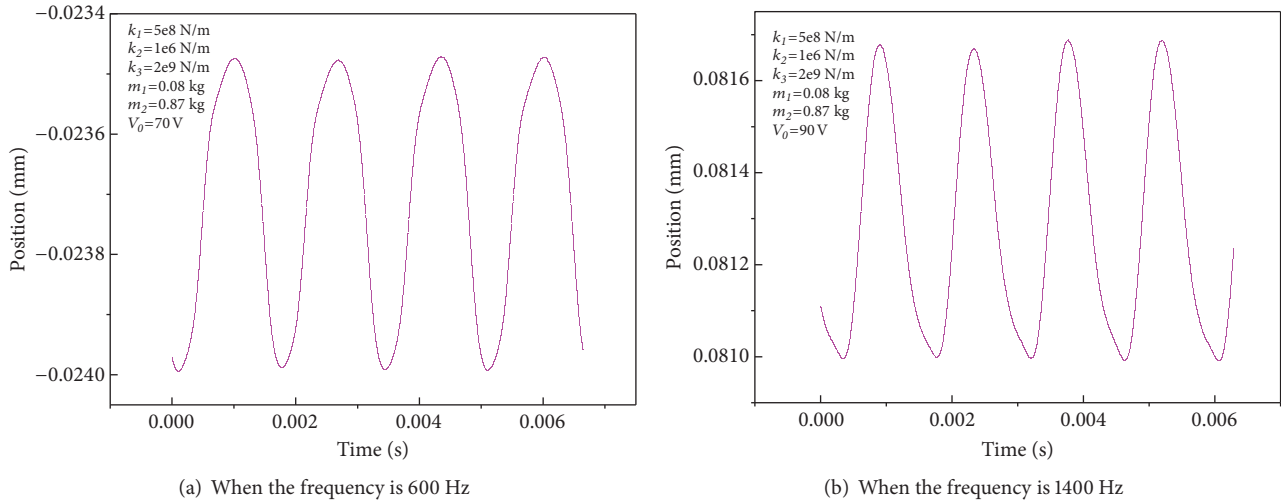


FIGURE 13: Normal vibration displacement curves.

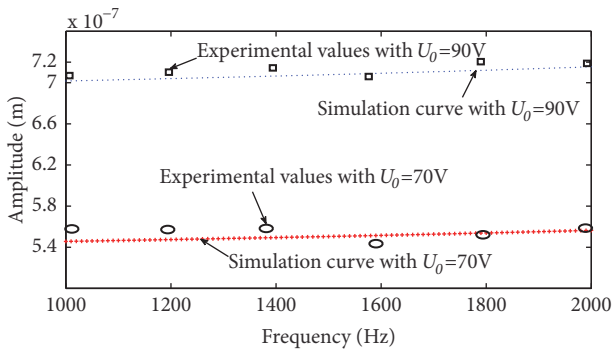


FIGURE 14: Normal amplitude–frequency response characteristic.

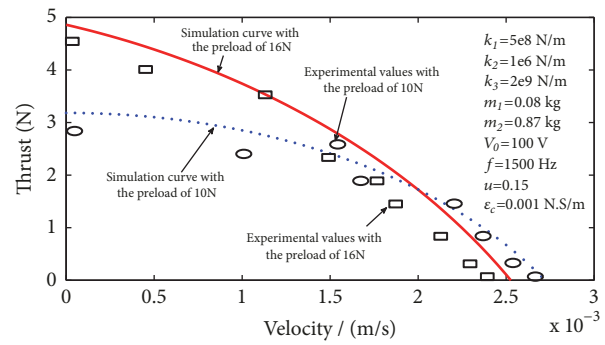


FIGURE 16: Comparison of simulation and experimental results.

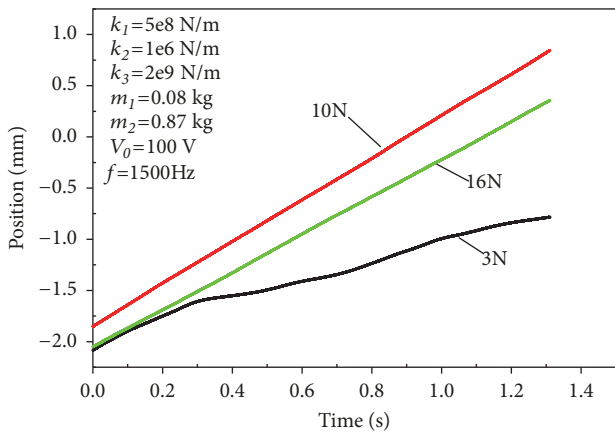


FIGURE 15: Displacement with different preloads.

and mechanical output characteristics of the motor. The simulation and experimental results show that the stator drive foot of the motor has stable normal vibration displacement output characteristics. In noncontact and contact phases, the value of the longitudinal amplitude is significantly affected by

the mass of the counterweight and minimally by the stiffness of the preloading spring. Under the same experimental conditions, the value of the normal amplitude in the noncontact phase varies from $0.5 \mu\text{m}$ to $0.8 \mu\text{m}$, whereas the value of the normal amplitude in the contact phase varies from $0.05 \mu\text{m}$ to $0.15 \mu\text{m}$.

The microscopic kinematic model for stator protruding section and the interface friction model for motor system are produced. The simulation results show that the increase in contact stiffness and normal amplitude can make the mechanical characteristics of the motor hard and the output force of the motor be improved. The experimental results show that the microscopic dynamic model of the motor can predict the mechanical output characteristics of the motor, which can provide reference for the theoretical study of non-resonance piezoelectric motors. From the simulation analysis and experimental results, when the preload is 16 N, the maximum thrust of the motor is 4.2 N, the maximum velocity is 2.52 mm/s, and the displacement resolution is up to $0.1 \mu\text{m}$.

Data Availability

The data used to support the findings of this study are available from the corresponding author upon request.

Conflicts of Interest

The authors declare that they have no conflicts of interest.

Acknowledgments

This work is supported by the following funding organizations in China: the National Natural Science Foundation of China (Grant No. 51405420, 51505161, and 51375224), the Natural Science Foundation of Jiangsu Province (Grant No. BK20140474), Natural Science Research Projects in Jiangsu Higher Education Institutions (18KJB460030), Natural Science Foundation of Fujian Province (No. 2016J01236), and the sponsorship of Jiangsu Oversea Research and Training Program for University Prominent Young & Middle-aged Teachers, Blue Project of Jiangsu Province.

References

- [1] K. Uchino, "Piezoelectric ultrasonic motors: Overview," *Smart Materials and Structures*, vol. 7, no. 3, pp. 273–285, 1998.
- [2] T. Hemsell and J. Wallaschek, "Survey of the present state of the art of piezoelectric linear motors," *Ultrasonics*, vol. 38, no. 1, pp. 37–40, 2000.
- [3] Y. Zhao, S. Yuan, X. Chu, S. Gao, Z. Zhong, and C. Zhu, "Ultrasonic micro-motor with multilayer piezoelectric ceramic and chamfered driving tips," *Review of Scientific Instruments*, vol. 87, no. 9, p. 095108, 2016.
- [4] W. Dong, H. Li, and Z. Du, "A planar nano-positioner driven by shear piezoelectric actuators," *AIP Advances*, vol. 6, no. 8, p. 085104, 2016.
- [5] S.-T. Ho and S.-J. Jan, "A piezoelectric motor for precision positioning applications," *Precision Engineering*, vol. 43, pp. 285–293, 2016.
- [6] H. Guo, G. Xiao, N. Mrad, J. Albert, and J. Yao, "Wavelength interrogator based on closed-loop piezo-electrically scanned space-to-wavelength mapping of an arrayed waveguide grating," *Journal of Lightwave Technology*, vol. 28, no. 18, pp. 2654–2659, 2010.
- [7] V. Koledov, V. Shavrov, S. Von Gratowski, S. Petrenko, A. Irzhak, and A. Shelyakov, "Practical system for nanomanipulation," in *Proceedings of the 4th International Conference on Manipulation, Manufacturing and Measurement on the Nanoscale, 3M-NANO 2014*, pp. 316–320, Taiwan, October 2014.
- [8] L. Wang, C. Shu, Q. Zhang, and J. Jin, "A novel sandwich-type traveling wave piezoelectric tracked mobile system," *Ultrasonics*, vol. 75, pp. 28–35, 2017.
- [9] K. Lee, D.-K. Lee, S. Borodinas, P. Vasiljev, S. Nahm, and S.-J. Yoon, "Analysis of shaking beam actuator for piezoelectric linear ultrasonic motor," *IEEE Transactions on Ultrasonics, Ferroelectrics and Frequency Control*, vol. 51, no. 11, pp. 1508–1513, 2004.
- [10] P. Vasiljev, S. Borodinas, R. Bareikis, L. Vasiljeva, and A. Irzhikевичius, "The stator of rotating type piezo-motor based on "shaking beam" actuator," *Solid State Phenomena*, vol. 113, pp. 203–206, 2006.
- [11] S. Borodin, J. Kim, H. Kim, P. Vasiljev, and S. Yoon, "Nano-Positioning System Using Linear Ultrasonic Motor with "Shaking Beam"," *Journal of Electroceramics*, vol. 12, no. 3, pp. 169–173, 2004.
- [12] Y. Shi, Y. Li, and C. Zhao, "Optimum design of a linear ultrasonic motor based on in-plane modes," in *Proceeding of the Chinese Society for Electrical Engineering*, vol. 28, pp. 56–60, 2008.
- [13] X. Chen, W. Huang, and Y. Wang, "Vibration characteristics of the stator of dynamic friction type linear piezoelectric stack motors," *Zhendong Ceshi Yu Zhenduan/Journal of Vibration, Measurement and Diagnosis*, vol. 34, no. 5, pp. 960–966, 2014.
- [14] X. Li, Z. Yao, Q. Lv, and Z. Liu, "Modeling stick-slip-separation dynamics in a bimodal standing wave ultrasonic motor," *Journal of Sound and Vibration*, vol. 382, pp. 140–157, 2016.
- [15] P. L. Moal, E. Joseph, and J.-C. Ferniot, "Mechanical energy transduction in standing wave ultrasonic motors: Analytical modelling and experimental investigations," *European Journal of Mechanics - A/Solids*, vol. 19, no. 5, pp. 849–871, 2000.
- [16] J. Wallaschek, "Contact mechanics of piezoelectric ultrasonic motors," *Smart Materials and Structures*, vol. 7, no. 3, pp. 369–381, 1998.
- [17] Y. Shi, C. Zhao, and J. Zhang, "Contact analysis and modeling of standing wave linear ultrasonic motor," *Journal of Wuhan University of Technology-Mater. Sci. Ed.*, vol. 26, no. 6, pp. 1235–1242, 2011.
- [18] W. Bowden, I. R. Hill, P. E. Baird, and P. Gill, "Note: A high-performance, low-cost laser shutter using a piezoelectric cantilever actuator," *Review of Scientific Instruments*, vol. 88, no. 1, p. 016102, 2017.
- [19] X. Cao and J. Wallaschek, "Modelling and analysis of dynamic contact problems in travelling wave ultrasonic motors," *ZAMM: Zeitschrift für Angewandte Mathematik und Mechanik*, vol. 76, no. 5, pp. 93–94, 1996.
- [20] H. W. Zhao, *Basic theory and experimental study on inchworm-type piezoelectric actuator*, Jilin University, Jilin, 2006.
- [21] X. Zhao, Study on Dynamic Model and Performance Simulation of Rotating Traveling Wave, Ultrasonic Motor, pp. 40–41, 2000.

